CrossMark

Advanced TEM characterization of oxide nanoparticles in ODS Fe–12Cr–5Al alloys

Kinga A. Unocic[1,*], Bruce A. Pint[1], and David T. Hoelzer[1]

[1] *Oak Ridge National Laboratory, Oak Ridge, TN 37831, USA*

ABSTRACT

The oxide nanoparticles present in three oxide-dispersion-strengthened (ODS) Fe–12Cr–5Al alloys containing additions of (1) Y_2O_3 (125Y), (2) $Y_2O_3 + ZrO_2$ (125YZ), and (3) $Y_2O_3 + HfO_2$ (125YH), were investigated using transmission and scanning transmission electron microscopy. In all three alloys nano-sized (<3.5 nm) oxide particles distributed uniformly throughout the microstructure were characterized using advanced electron microscopy techniques. In the 125Y alloy, mainly Al_2O_3 and yttrium–aluminum garnet (YAG) phases ($Y_3Al_5O_{12}$) were present, while in the 125YZ alloy, additional Zr(C,N) precipitates were identified. The 125YH alloy had the most complex precipitation sequence whereby in addition to the YAG and Al_2O_3 phases, Hf(C,N), $Y_2Hf_2O_7$, and HfO_2 precipitates were also found. The presence of HfO_2 was mainly due to the incomplete incorporation of HfO_2 powder during mechanical alloying of the 125YH alloy. The alloy having the highest total number density of the oxides, the smallest grain size, and the highest Vickers hardness was the 125YZ alloy indicating, that $Y_2O_3 + ZrO_2$ additions had the strongest effect on grain size and tensile properties. High-temperature mechanical testing will be addressed in the near future, while irradiation studies are underway to investigate the irradiation resistance of these new ODS FeCrAl alloys.

Introduction

Mechanically alloyed oxide dispersion strengthened (ODS) ferritic alloys, containing nano-sized oxide dispersions, are materials of interest for fusion blanket concepts in high-operating temperature DEMO-type fusion reactors due to their superior creep strength and resistance to irradiation when compared to conventional ferritic steels [1–3]. There are several criteria that these alloys must meet to be considered for high temperature fusion reactor applications, such as corrosion, strength, ductility, fracture toughness, and microstructural stability at high temperatures. Such ODS ferritic alloys will need to be compatible with both Pb–Li and He since DEMO-type fusion reactors will use eutectic Pb–Li and He dual coolants for higher operating temperatures. In general, the corrosion resistance of Al-free ODS alloys can be improved by increasing the Cr level; however, in alloys with higher Cr contents, irradiation damage can induce the

---

formation of the alpha-prime (α') phase, subsequently causing radiation embrittlement [4]. Thus, lowering the Cr content and modifying the material's composition with Al is a potential route towards improved corrosion resistance [5–7]. Unfortunately, the addition of Al is known to have a negative effect on the mechanical properties of the alloy due to formation of larger sized oxide particles with a lower number density [7] and Al will also affect the ductile–brittle transition temperature due to cross-slip inhibition [8]. However, the addition of group IVB elements has been suggested by Furukawa et al. [9] to help balance the mechanical properties with good corrosion resistance. It was shown by Dou et al. [10] that the addition of Zr to Fe–15Cr–2W–0.1Ti–4Al–0.35Y_2O_3 (wt%) improved the oxide dispersion morphology and coherency of the nano-size oxide particles with the matrix, which enhanced the mechanical properties. Conversely, the addition of other elements, e.g., Y, Hf, Zr, or Ti, caused the formation of different oxide phases depending on the alloying element. For example, in ODS alloys with a composition of 16Cr–4Al–2W–0.35Y_2O_3, $YAlO_3$ was found, while when additions of Zr or Hf (not clearly specified how they were added: atomized or as powder particles) were used, the oxide particles were identified using selected area electron diffraction (SAED) analysis as $Y_2Zr_2O_7$ and $Y_2Hf_2O_7$, respectively [11]. Often, electron diffraction analysis is not sufficient to identify the exact phase of the oxide nanoparticles, and many particles are too small to be examined. Thus, high-resolution transmission electron microscopy (HRTEM) can be used to further interrogate the nanoparticles. For example, three different types of oxide nanoparticles were identified via HRTEM in a Fe–15Cr–2W–0.1Ti–4Al–0.35Y_2O_3 ODS alloy [10]; coherent trigonal δ-phase $Y_4Zr_3O_{12}$ oxides, semi-coherent orthorhombic Y_2TiO_5 and tetragonal or cubic ZrO_2 oxides. Currently, a number of institutions are developing new ODS FeCrAl alloys; however, small changes in the mechanical alloying procedure and/or the alloy composition can strongly affect the final microstructure (including the formation of different oxides and precipitates) and the mechanical properties of the alloy [11–14]. Thus, it is crucial to identify all the oxide particles and precipitates formed in ODS alloys as a function of processing variables employed and alloying elements used should be investigated to improve our understanding of the material's mechanical and corrosion behavior.

The objective of the present work was to perform a detailed microstructural characterization of mechanically alloyed ODS Fe–12Cr–5Al with the following oxide additions: (1) Y_2O_3, (2) $Y_2O_3 + ZrO_2$, and (3) $Y_2O_3 + HfO_2$, in order to identify the size scale, morphology, distribution, crystal structure, and chemical composition of oxide phases present in the alloys. HRTEM characterization was performed on the three as-extruded alloys after mechanical alloying and results showed that both the grain size and precipitate type varied between the three alloys.

Experimental procedure

Three ODS FeCrAl alloys were produced with high kinetic energy ball milling (CM08 Zoz Simoloyer) from 1 kg of pre-alloyed argon gas-atomized powder feed stock (Fe–12Cr–5Al wt% from ATI Powder Metals) together with the following oxide additions (and alloy designation given in parentheses): (1) Y_2O_3 (125Y), (2) $Y_2O_3 + ZrO_2$ (125YZ), and (3) $Y_2O_3 + HfO_2$ (125YH). Ball milling was carried out for 40 h under an argon atmosphere. Afterward, the powders were placed in mild steel cans and heat treated for 1 h at 950 °C followed by hot extrusion. The chemical composition (in at%) of the as-extruded material is presented in Table 1. The 125Y alloy contained the highest C and N impurities and lowest Cr and Al content and also had the lowest O level due to the addition of only Y_2O_3 powder as compared to 125YZ and 125YH, which in addition, contained ZrO_2 and HfO_2, respectively. For comparison, the composition of PM2000^{TM}, a commercially produced ODS alloy by Plansee, is also included in Table 1.

The as-extruded and aged microstructures were characterized using a Hitachi S4800 scanning electron microscope (SEM) equipped with energy dispersive X-ray spectroscopy (EDS). The average grain size was obtained by the line intercept method in terms of the 95 % confidence interval around the mean. Specimens for TEM analysis were prepared by focused ion beam (Hitachi model NB5000 FIB-SEM) using the in situ lift-out method from polished metallographic samples of the extruded ODS FeCrAl heats. A Philips model CM200 FEG-TEM/scanning TEM (STEM) with EDS and electron energy loss spectroscopy (EELS) was used for microstructural and compositional analyses. Bright-field (BF) and high-angle annular-dark field

Table 1 Chemical composition (at%) determined by inductively coupled plasma atomic emission spectroscopy (ICP-AES)

Materials	Fe	Cr	Al	Y	N	C	S	O	Others
FeCrAl + Y_2O_3	78.3	11.5	9.3	1122	1705	1661	33	2763	
FeCrAl + Y_2O_3 + HfO_2	77.5	11.8	9.4	1006	413	963	16	7495	0.20Hf–0.006Zr
FeCrAl + Y_2O_3 + ZrO_2	77.8	11.6	9.5	1062	603	1092	16	6293	0.003Hf–0.17Zr
PM2000	68.9	19.1	10.5	2280	319	61	13	8056	0.06Mn–0.02Ni–0.03P–0.04Si–0.52Ti

Values for Y, O, N, C, S in ppma

(HAADF)-STEM and energy-filtered TEM (EFTEM) imaging methods were used in the microstructural investigations. For HR STEM imaging, a JEOL 2200FS aberration-corrected STEM operating at 200 kV with 0.7 Å resolution in STEM mode was used, which is equipped with a CEOS C_s-corrector and a Bruker XFlash® 6|30 silicon drift detector (SDD) with a 30 mm^2 active chip area. A FEI Talos F200X operated at 200 kV was also used, which is equipped with an extreme field emission gun electron source and Super-X EDS system for chemical analysis. Electron diffraction patterns and fast Fourier transforms (FFTs) from HRTEM/HRSTEM images were used for crystal structure identification of the oxide particles present in the three ODS alloys. The hardness tests were performed on as-extruded specimens using Vickers test with 200 or 500 g loads depending on the hardness of the material.

Results

Grain structure

Figure 1 shows the microstructures of the as-extruded alloys using HAADF-STEM imaging. The grain morphologies showed variations between the three alloys. The average grain length (parallel to the extrusion direction), average grain width (normal to the extrusion direction), and grain aspect ratio (GAR) for each alloy were 0.83 ± 0.17 μm, 0.56 ± 0.09 μm, and 1.48 ± 0.06 for 125Y, respectively, 0.27 ± 0.06 μm, 0.17 ± 0.02 μm, and 1.59 ± 0.15 for 125YZ, respectively, and 0.70 ± 0.16 μm, 0.39 ± 0.06 μm, and 1.79 ± 0.12 for 125YH respectively [15, 16]. Representative SAED patterns shown in Fig. 1c, f, i were obtained with the same SA aperture size to reflect the grain sizes and showed more continuous diffraction rings for 125YZ (Fig. 1f), which had the smallest grain size, while more speckled rings for 125Y (Fig. 1c) and 125YH (Fig. 1i) alloys, indicative of a larger grain size. The

SAED observations agree with the results from the grain size measurements.

Particle size, distribution, and identification

Each alloy contained oxide particles of several different phases (Fig. 1). These variations among the particles can be distinguished based on the atomic number (Z)-contrast in the HAADF-STEM images (Fig. 1b, e, h). Bimodal particle sizes were observed in both 125Y and 125YZ alloys, while a tri-modal particle size was observed in 125YH. The total number density of particles were measured in the ODS alloys by counting all particles in the field of view (regardless of the size and location) in HAADF-STEM images and using thickness values based on the average of t/λ images obtained by EFTEM for each alloy. The total number density of particles was 1.4×10^{23} m^{-3} for 125Y, 2.5×10^{23} m^{-3} for 125YZ, and 2.3×10^{23} m^{-3} for 125YH. In all three alloys, a high number density of small nanoparticles ($\sim$3 nm) distributed uniformly throughout the matrix were observed, which exhibited dark contrast relative to the surrounding matrix in HAADF-STEM images (Fig. 1b, e, h). The presence of $\sim$3 nm particles was confirmed by EFTEM imaging (Fig. 2) with the contrast intensity profiles generated across the particles demonstrating their size (Fig. 2d–f). The comparison of Fe-jump ratio and HAADF-STEM imaging indicated that the techniques complemented each other. Similar particles with dark contrast in the HAADF-STEM images but with larger sizes ($d \cong 10.6 \pm 11.2$ nm for 125Y, $d \cong 31 \pm 18.2$ nm for 125YH, and $d \cong 10.2 \pm 5.8$ nm for 125YZ) were found near and/or along grain boundaries (see arrow in Fig. 1e).

Additionally, randomly distributed oxides, ranging in size from 6 to 25 nm, were observed in alloy 125Y that showed contrast variations (Z-contrast
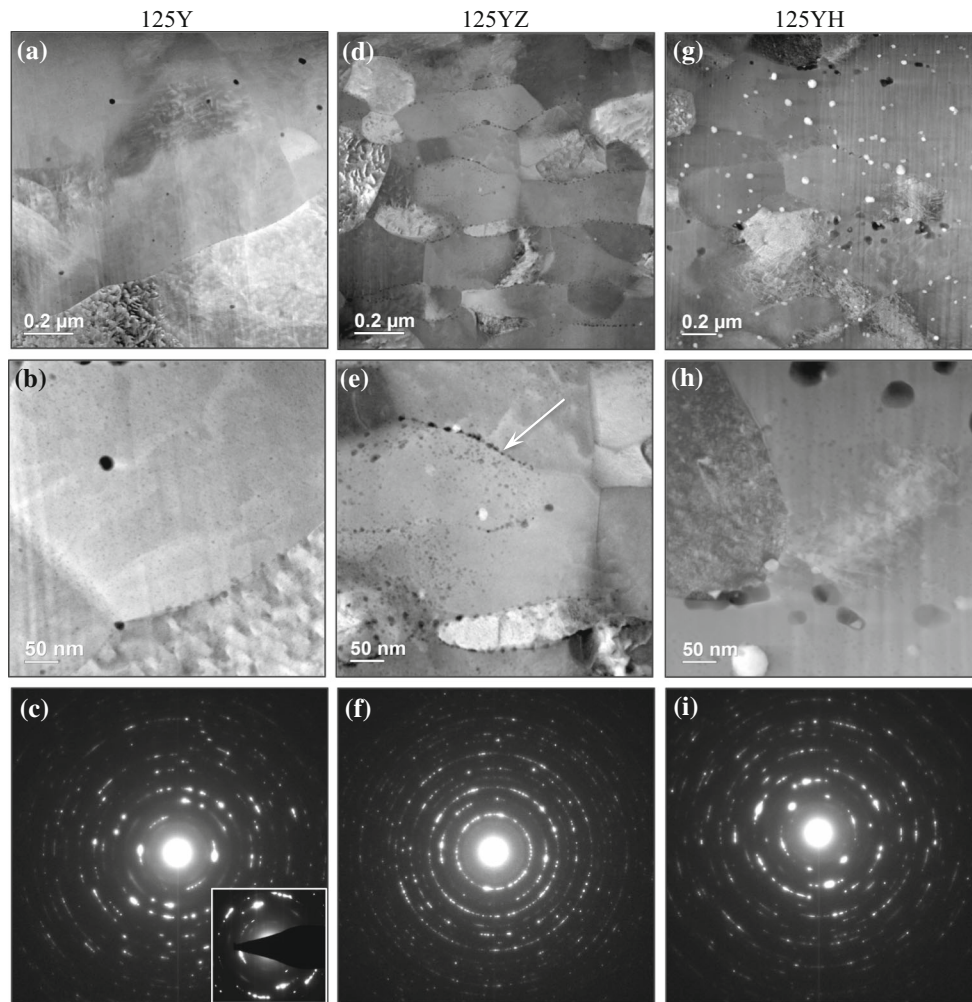
Figure 1 HAADF-STEM images of 125Y (**a**, **b**), 125YZ (**d**, **e**), and 125YH (**g**, **h**) with corresponding diffraction patterns (**c**, **f**, **i**) after being mechanically alloyed and extruded at 950 °C.

image) indicating that they consisted of two phases. In Fig. 3a, the HAADF-STEM image shows contrast variations across such an oxide particle. The compositional variation was confirmed by EDS elemental maps (Fig. 3b) and EDS point analysis shown in Fig. 3c: the darker contrast within the oxide particle (EDS spectrum #3) corresponds with Al-enrichment and O (Al_2O_3), while the lighter gray contrast region (EDS spectrum #2) shows Y-enrichment (higher Z) in addition to Al and O. For comparison, EDS spectrum #1 was generated from the matrix and shows no Y, e.g., the Y signal clearly is associated with the oxide precipitate. Furthermore, the SAED pattern acquired from a large area of 125Y (Fig. 1c) showed additional reflections to the body-centered cubic (BCC) Fe matrix consistant with the cubic $Y_3Al_5O_{12}$ [yttrium–aluminum garnet (YAG) phase] with, $Ia\bar{3}d$ space group and $a = 12.0089$ nm and $\alpha = \beta = \gamma = 90°$. The measured and ICDD (PDF# 00-033-0040) values of the inter-planar distances (*d*) are presented in Table 2. Identification of the Y-rich-dark contrast particles observed in HAADF-STEM images was also carried out using FFTs patterns (Fig. 4b) generated from the high-resolution BF-STEM images (Fig. 4a). Table 3 shows the measured inter-planar distances and angles of the particle with ICDD values. These results are consistent with the cubic $Y_3Al_5O_{12}$ (YAG phase).

In the 125YZ alloy, in addition to the small nano-size oxide particles and the large darker contrast (two phases) particles, there were also particles showing bright contrast that were 11.3 ± 5.5 nm in size, which sometimes co-existed with the darker contrast oxide particles (Figs. 5, 6). EDS analysis of these particles (Figs. 5, 6c) showed that part of the bright contrast
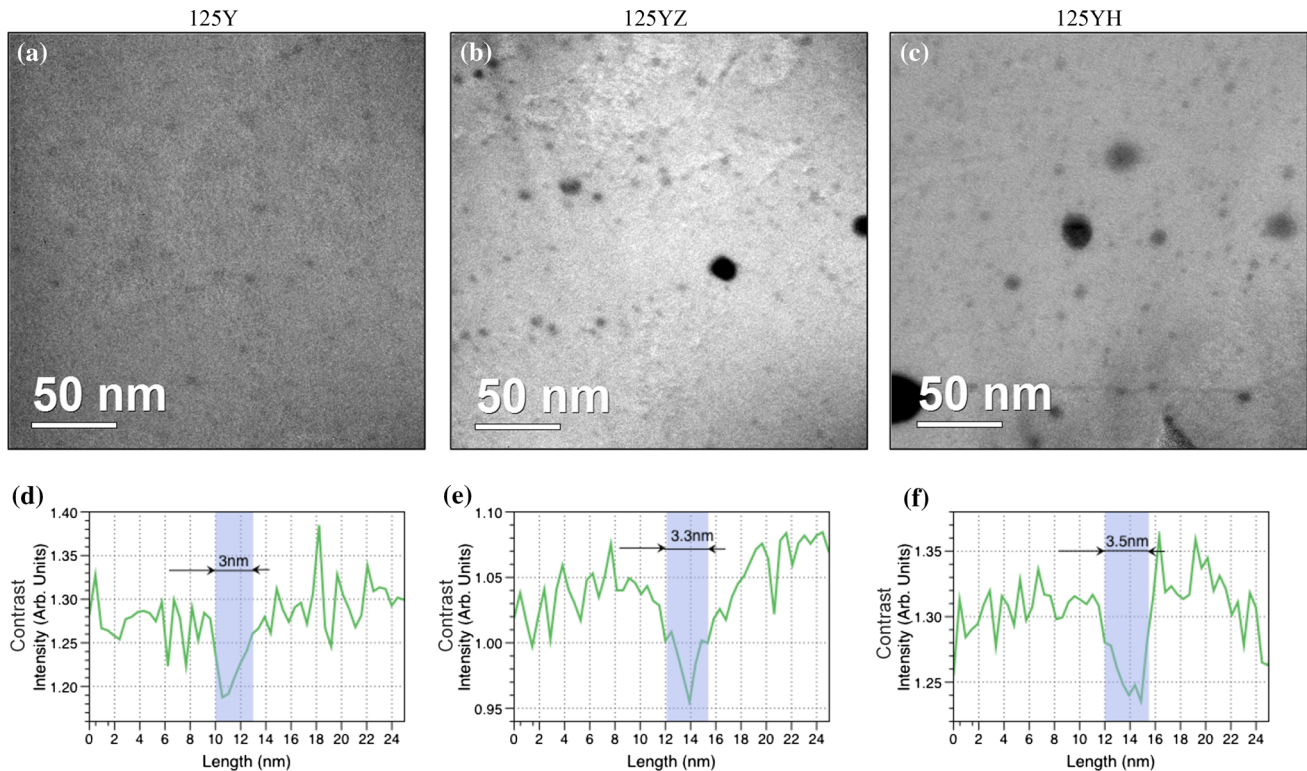
Figure 2 Fe-jump ratio images for **a** 125Y, **b** 125YZ, and **c** 125YH alloys with examples of the contrast intensity plots (**d**–**f**) generated across a particle to show their size.

was enriched in Zr, while the other part (darker contrast) of the particle was Al- and Y-enriched, again consistent with the YAG phase. A critical finding of this study is that Zr did not react with the Y and Al-rich oxides. The proximity of the Zr and Al/Y signals in the particle shown in Fig. 6 is actually due to separate overlapping particles, and does not result from a mixed composition. Further identification of these Zr-rich (particle with bright contrast in HAADF-STEM image) particles was also carried out using HR HAADF-STEM imaging (Fig. 6a) and corresponding FFT analysis (Fig. 6b). Table 4 shows the measured and ICDD (PDF# 00-020-0684) inter-planar distances and angles of the particle. The diffraction data are consistent with cubic Zr(C,N) phase, (confirmed via EDS), with the $Fm\bar{3}m$ space group, unlike trigonal δ-phase $Y_4Zr_3O_{12}$ ($R\bar{3}$) as was found by others [10].

The precipitation of oxide particles in 125YH alloy was more complex. The HAADF-STEM imaging analysis (Fig. 7) showed large (>100 nm) randomly distributed particles exhibiting bright contrast (Fig. 7a) that were often associated with particles

exhibiting dark contrast (>70 nm) in HAADF-STEM. Both phases based on contrast were identified using a combination of EDS and FFT/SAED analysis. As shown in EDS point spectrum #1 (Fig. 7b) the particle with bright contrast was enriched in Hf (high Z) and was identified using electron diffraction analysis as monoclinic HfO_2 with the $P2_1/c$ space group and a Hf/O ratio of 5.2 (quantified from the EDS spectrum), which is close to the theoretical Hf/O ratio of 5.6 for HfO_2. The EDS spectrum #2 acquired from the large particle exhibiting dark contrast showed primarily energy peaks for Al and O (with some Fe signal from the matrix), with neither Hf nor Y was detected. The Al/O ratio was 1.47 and the oxide particle was identified as Al_2O_3. The Al content is slightly higher than in a perfect ratio of Al/O for Al_2O_3 being 1.12. This small variation might be due to the interference of the matrix with the oxide (e.g., matrix beneath the oxide particle confirmed by Fe energy peak in the spectrum 2) affecting the measurement.

Particles exhibiting bright contrast (high Z) in HAADF-STEM images with a size of 27.8 ± 19.1 nm were also found in the matrix of alloy 125YH and

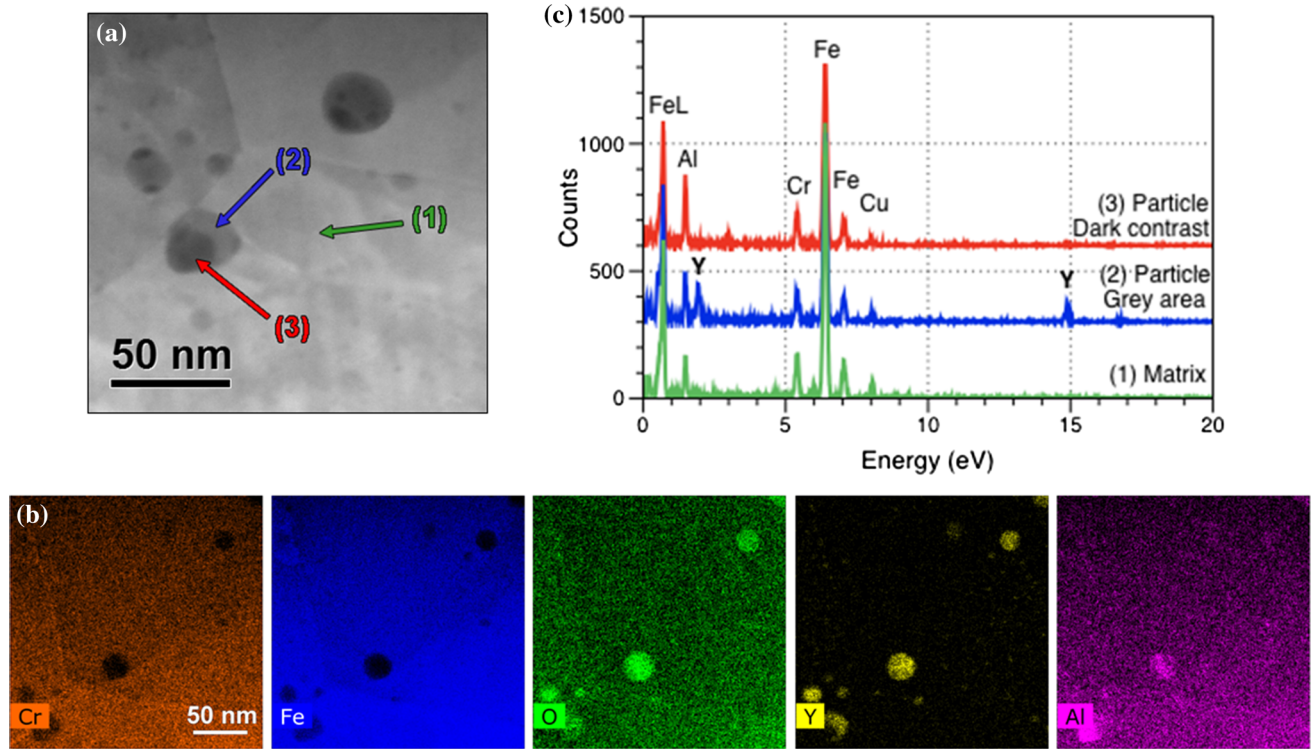**Figure 3 a** HAADF-STEM image of 125Y alloy with **b** EDS elemental maps and **c** EDS point spectra generated from co-precipitated oxide particles shown in **a**; dark contrast side is Al-rich with no Y (Al_2O_3) (spectrum #3), while lighter contrast part is Al- and Y-rich (YAG phase) (spectrum #3). For reference EDS spectrum #1 generated from the matrix is also shown.

EDS analysis (Fig. 8) showed that these particles are composed of Hf, C, and N. Further detailed phase identification was carried out and Fig. 9a shows an example of these particles in the HR BF-STEM image with the corresponding FFT (Fig. 9b). The measured inter-planar distances and angles of the particle are given in Table 5. The results are consistent with the cubic Hf(C,N) phase with space group $Fm\bar{3}m$ matching ICDD (PDF$^{\#}$ 01-080-4476) file. Small particles with dark contrast were also revealed by HAADF-STEM imaging revealed small dark contrast oxide particles enriched in Al and Y (EDS in Fig. 8b), which further agrees with EFTEM results shown previously by Fe-jump ratio map (Fig. 2c). EDS analysis showed that not all nano-size oxides are alike. Most of oxide nanoparticles in alloy 125YH were YAG phase (Y, Al, and O-rich), while some were enriched in Y, Hf, and O (Figs. 8, 10b), which exhibited gray contrast in HAADF-STEM image. This can be clearly seen in Hf EDS map, where in addition to Hf(C,N), the Hf signal also corresponds with small (4.8 ± 1.3 nm) oxides, which are also associated with Y and O as shown in the EDS maps. This suggests the

existence of $Y_2Hf_2O_7$ oxides. Higher magnification EDS maps generated from the co-nucleated oxide particles are shown in Fig. 10, where (Hf, Y) oxide is evident. The EDS elemental maps (Fig. 10b) confirmed enrichment of Y and Hf in the gray area of the particle in the HAADF-STEM image, while only Al and O were detected in the dark contrast area. An example of a HR BF-STEM image of co-precipitated Y and Hf-rich oxide is shown in Fig. 10c. FFT generated from the image (Fig. 10d) and the measured inter-planar distances and angles from the gray contrast particle are shown in Table 6. FFT shows (111) and (220) reflections with a 35° angle between them. These measurements are consistent with the pyro-chlore structure of cubic $Y_2Hf_2O_7$ with $Fd\bar{3}m$ space group from ICSD (PDF$^{\#}$ 04-001-9353) file.

The last type of oxide particle found in 125YH alloy was a complex two-phase oxide ($d \cong 14.5$ nm) showing either dark-gray or gray-bright contrast areas in the HAADF-STEM image (Fig. 11a, arrows). These oxides (20–60 nm) were slightly larger than those (~20 nm) found in the 125Y and 125YZ alloys and were not uniform in composition based on the

Table 2 Measured and calculated inter-planar distances (d) for 125Y, 125YZ, and 125YH alloys

$d_{measured}$ (Å)	d_{tabled} (Å)	Reflections	Stoichiometry	Space groups
125Y alloy				
2.959	3.002	(400)	$Y_3Al_5O_{12}$	$Ia\overline{3}d$ (230)
2.414	2.452	(422)	$Y_3Al_5O_{12}$	$Ia\overline{3}d$ (230)
2.023	2.027	(101)	Fe	$Im\overline{3}m$ (229)
1.474	1.478	(741)	$Y_3Al_5O_{12}$	$Ia\overline{3}d$ (230)
125YZ alloy				
2.621	2.560	(200)	ZrO_2	$Fm\overline{3}m$ (225)
	2.667	(111)	ZrO	$Fm\overline{3}m$ (225)
	2.617	(002)	ZrO_2	$P2_1/c$ (14)
2.097	2.027	(101)	Fe	$Im\overline{3}m$ (229)
	2.122	(440)	$Y_3Al_5O_{12}$	$Ia\overline{3}d$ (230)
	2.020	(211)	ZrO_2	$P2_1/c$ (14)
	2.024	(104)	$YAlO_3$	$P6_3/mmc$ (194)
1.489	1.433	(200)	Fe	$Im\overline{3}m$ (229)
	1.478	(741)	$Y_3Al_5O_{12}$	$Ia\overline{3}d$ (23)
	1.481	(222)	ZrO_2	$Fm\overline{3}m$
1.212	1.281	(400)	ZrO_2	$Fm\overline{3}m$ (225)
	1.213	(941)	$Y_3Al_5O_{12}$	$Ia\overline{3}d$ (230)
	1.204	(210)	$YAlO_3$	$P6_3/mmc$ (194)
	1.213	($\overline{1}$41)	ZrO_2	$P2_1/c$ (14)
1.057	1.013	(202)	Fe	$Im\overline{3}m$ (229)
	1.047	(422)	ZrO_2	$Fm\overline{3}m$ (225)
125YH alloy				
2.581	2.575	(400)	$Y_2Hf_2O_7$	$Fd\overline{3}m$ (227)
	2.561	(332)	$Y_3Al_5O_{12}$	$Ia\overline{3}d$ (230)
	2.591	(020)	HfO_2	$P2_1/c$ (14)
	2.600	(200)	$Y_2Hf_2O_7$	$Fm\overline{3}m$ (225)
2.116	2.103	(422)	$Y_2Hf_2O_7$	$Fd\overline{3}m$ (227)
	2.122	(440)	$Y_3Al_5O_{12}$	$Ia\overline{3}d$ (230)
1.498	1.433	(200)	Fe	$Im\overline{3}m$ (229)
	1.478	(741)	$Y_3Al_5O_{12}$	$Ia\overline{3}d$ (230)
1.211	1.214	(822)	$Y_2Hf_2O_7$	$Fd\overline{3}m$ (227)
	1.213	(941)	$Y_3Al_5O_{12}$	$Ia\overline{3}d$ (230)
1.051	1.013	(202)	Fe	$Im\overline{3}m$ (229)

PDF files used: $Y_3Al_5O_{12}$ (225), 00-033-0040; $YAlO_3$ (194), 00-054-0621; ZrO_2 (225), 00-049-1642; ZrO_2 (14), 00-013-0307; ZrO (225), 00-020-0684; HfO_2 (14), 00-043-1017; $Y_2Hf_2O_7$ (225), 00-059-0532; $Y_2Hf_2O_7$ (227), and ICSD 153819

Z-contrast in the HAADF-STEM image (Fig. 11a). The darker contrast of the particles were enriched mainly in Al and O (most likely Al_2O_3) while the other part of the oxide (gray) was enriched in Y in addition to Al and O elements and appeared slightly brighter in contrast due to the presence of Y. The electron diffraction analysis (Fig. 11b) with the measured inter-planar distances and correlated {hkl} planes is summarized in Table 7 and is in close agreement with the cubic $Y_3Al_5O_{12}$ (YAG phase) with $Ia\overline{3}d$ matching ICDD (PDF# 33-0040). A summary of all of the oxides and particles identified in the three ODS FeCrAl alloys is presented in Table 8.

Hardness measurements

The Vickers hardness measurements were carried out on all three ODS FeCrAl alloys in the as-extruded
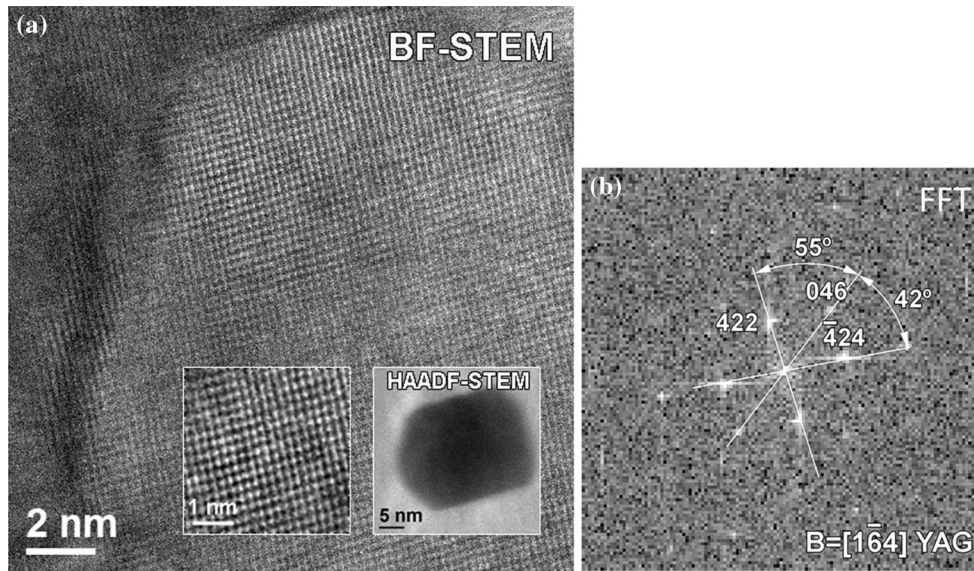
Figure 4 **a** High-resolution BF-STEM image (with zoom in inset) showing particle in 125Y that exhibited dark contrast in HAADF-STEM image (*inset* in 4a) with corresponding **b** FFT pattern showing the best fit and consistency for *d*-spacing and angles for YAG phase $Al_5Y_3O_{12}$ ($Ia\bar{3}d$).

Table 3 Measured and ICDD (PDF$^{\#}$ 00-033-0040) inter-planar distances (*d*) and angles (α) for particle with dark contrast in HAADF-STEM in 125Y alloy

d (Å)	$d_1(422)$	$d_2(\bar{4}24)$	$d_3(046)$	α_{13} (°)	α_{23} (°)	α_{12} (°)
Measured	2.959	2.414	1.474	55	42	83
$Al_5Y_3O_{12}$ (YAG)	3.002	2.452	(422)	55.5	42.3	82.2

condition and a summary of the hardness measurements is shown in Fig. 12. The highest Vickers hardness of 470 HV was measured for the 125YZ alloy, which had the smallest grain size. Alloy 125YH had a slightly lower hardness (420 HV), while the lowest hardness was measured for alloy 125Y (365 HV). For comparison measurements were also carried out on the commercial PM2000 alloy and the hardness value (356 HV) was lower than for all three new ODS FeCrAl alloys (Fig. 12).

Discussion

The oxide phases discovered in 125Y, 125YZ, and 125YH and their comparison to literature studies of other ODS FeCrAl alloys

It has been shown [9, 17] that the addition of HfO_2 and ZrO_2 bring the reduced strength of Al containing

ODS Fe-alloys back to the original strength of Al-free ODS ferritic steels. In our study, the main goal was to develop PbLi compatible alloys for fusion applications. Therefore, the purpose of the HfO_2 and ZrO_2 additions in 125YH and 125YZ, respectively, was to investigate any potential interactions of these oxide additives with Y_2O_3 to form complex oxide phases, like $Y_4Zr_3O_{12}$ and $Y_2Hf_2O_7$, and thereby force Al to remain in solid solution in the BCC Fe matrix to act as reservoir for surface scale (Al_2O_3) formation to improve the high-temperature oxidation behavior of the material. However, our results showed that $Y_3Al_5O_{12}$ (cubic, YAG) formed in all three alloys, exposing the high affinity between Al, Y, and O and that the addition of Hf or Zr did not prevent YAG formation. Formation of YAG precipitates in all three alloys might indicate that Y–Al oxide is the most stable and favorable phase.

In alloy 125YZ, no evidence for the formation $Y_2Zr_2O_7$, $Y_4Zr_3O_{12}$, or Y_6ZrO_{11} was found, as has been observed by others [11, 18]. Instead, based on
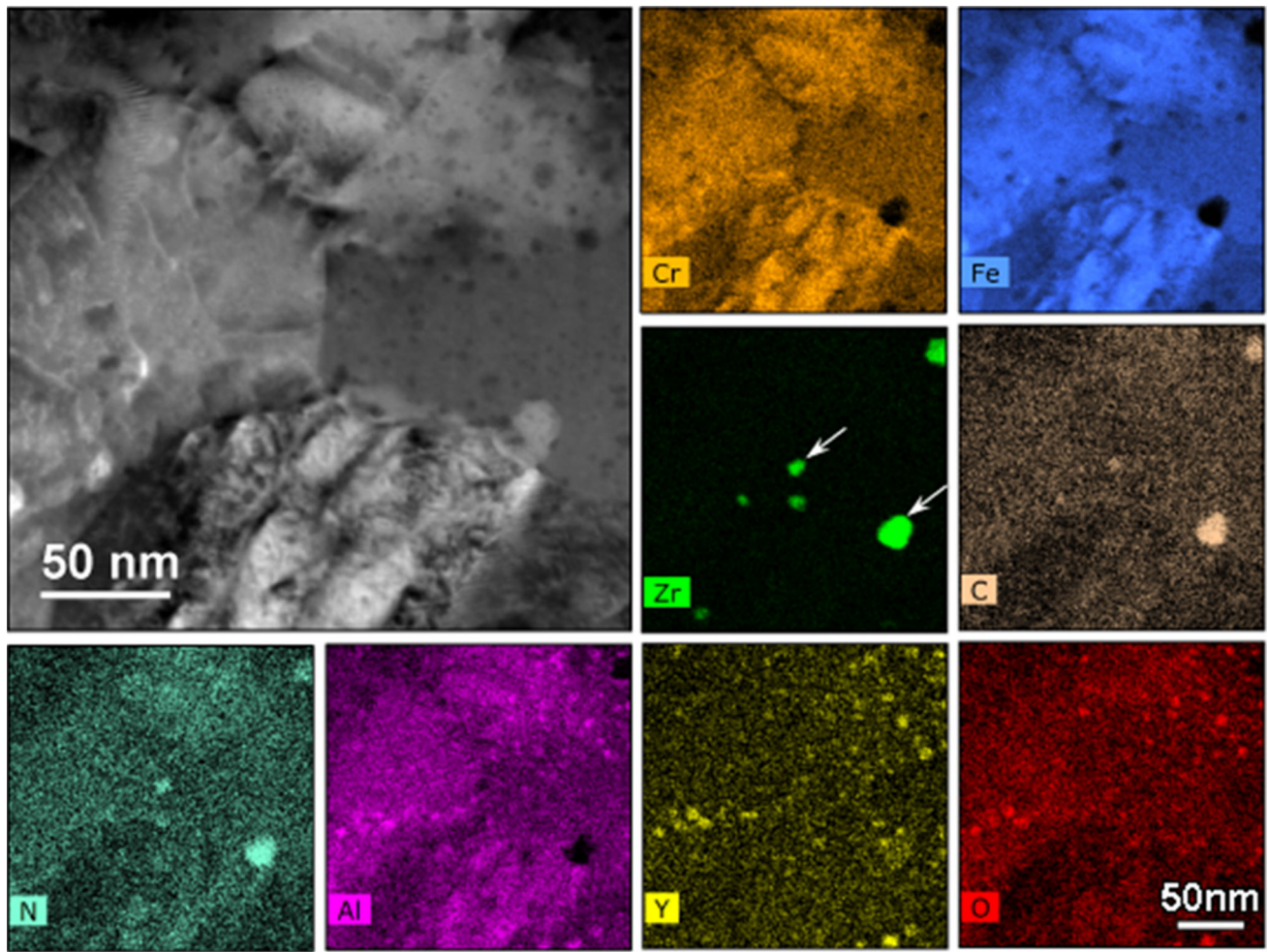
Figure 5 HAADF-STEM image of the 125YZ as-extruded (lift-out FIB) microstructure with corresponding EDS elemental maps of Cr, Fe, Zr, C, N, Al, Y, and O.

the electron diffraction analysis, the cubic Zr(C,N) phase was found in the present work. Since O tends to react with Zr to form cubic ZrO, which has a similar structure to the MX-type carbide with minor difference in lattice parameter [19]. This result suggests that the Zr(C,N) particles are MX-type carbides or carbo-nitride phases with possible enrichment of interstitial O since they are simply isomorphous phases with each other. This was established via EDS in conjunction with HR STEM analysis that confirmed the cubic crystal structure with the $Fm\bar{3}m$ space group. In addition, the Zr(C,N) particles often co-nucleated with Al_2O_3 particles, which has not commonly been observed and their stability needs to be investigated further.

In alloy 125YH, more complex phase reactions and precipitation sequence occurred compared to that of

125YZ, which is most likely due to the lower Hf solubility in the BCC Fe matrix compared to Zr [20]. The electron diffraction characterization provided evidence that all three cubic Hf(C,N), pyrochlore $Y_2Hf_2O_7$, and HfO_2 precipitates had co-nucleated with Al_2O_3, which was an unexpected result.

Previous research has shown that when both Al and Ti are present in the ODS alloy [14], various Y–Al complex oxides can form in addition to pyrochlore $Y_2Ti_2O_7$ depending on the differences in the processing and composition of the ODS ferritic steels. Usually their size is between 7 and 30 nm and their number density is lower (10^{20}–10^{22}) than in Al-free ODS alloys [14, 21–24]. A variety of Y–Al oxides have been previously identified in ODS alloys: $Y_4Al_2O_9$ (monoclinic, YAM) in PM2000 [25, 26], $YAlO_3$ (hexagonal, YAH) [27], $Y_4Al_3O_9$ (perovskite, YAP) in
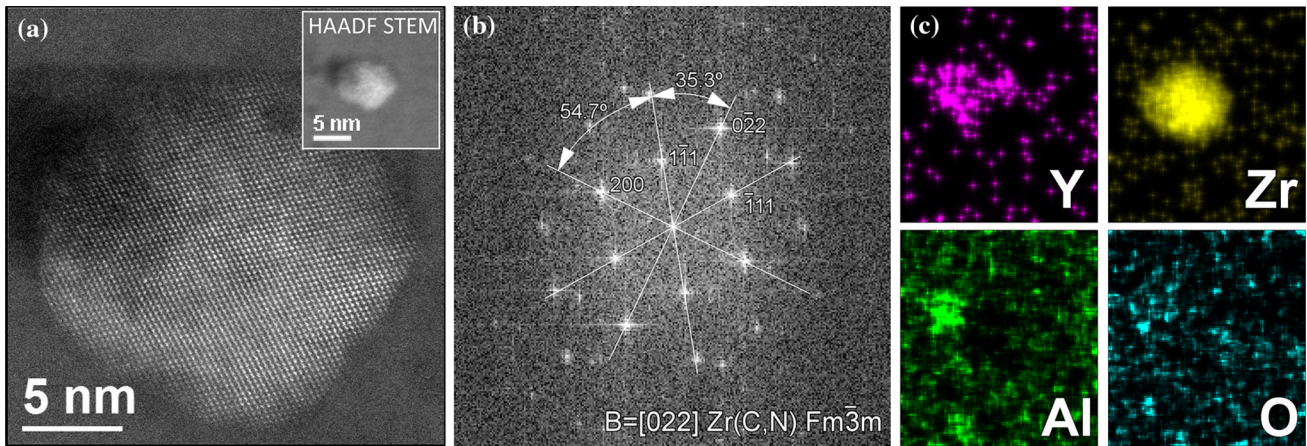
Figure 6 **a** High-resolution HAADF-STEM image of the Zr-rich particle formed in the 125YZ identified as Zr(C,N) with the $Fm\bar{3}m$ using **b** FFT and with corresponding **c** EDS Y, Zr, Al, and O elemental maps generated from oxide particle.

Table 4 Measured and ICDD (PDF$^{\#}$ 00-020-0684) inter-planar distances (*d*) and angle (*α*) for particle exhibited bright contrast in HAADF in 125YZ alloy

d (Å)	$d_1(1\bar{1}1)$	$d_2(200)$	$d_3(0\bar{2}2)$	α_{12} (°)	α_{23} (°)	α_{32} (°)
Measured	2.75	2.320	1.700	54.7	35.3	35.3
Zr(C,N)	2.667	2.310	1.633	54.7	35.3	35.3

PM2000 and K4 [14, 27, 28], $Y_3Al_5O_{12}$ (cubic, YAG) in PM2000 [27, 29, 30], and $Y_3Al_5O_{12}$ (tetragonal, YAT) in MA956 [26, 31]. Typically, ODS alloys with Y–Al oxides have lower mechanical properties than aluminum-free ODS alloys. However, when only Ti is present and no Al, pyrochlore $Y_2Ti_2O_7$ mainly forms [14], which strongly influences the strength of the material (strength increases) due to the smaller nanoparticle size, higher number density (1.3×10^{23} m^{-3}) [14], and more uniform distribution in the matrix [32]. This agrees with our findings, where mainly Y–Al nano oxides ($Y_3Al_5O_{12}$ YAG) and Al_2O_3 were found in 125Y alloy, and this alloy had lower hardness and mechanical properties due to the presence of the larger Al_2O_3. When either Zr or Hf was added to 125YZ or 125YH, respectively, a higher number density, more complex oxides (various type) oxides and more uniform distribution of particles and oxides were found in the ODS alloy, suggesting the advantageous effect of elemental additions from group IVB (e.g., Ti, Zr, Hf, Rf) [9].

Co-nucleation of oxides in 125Y, 125YZ, and 125YH

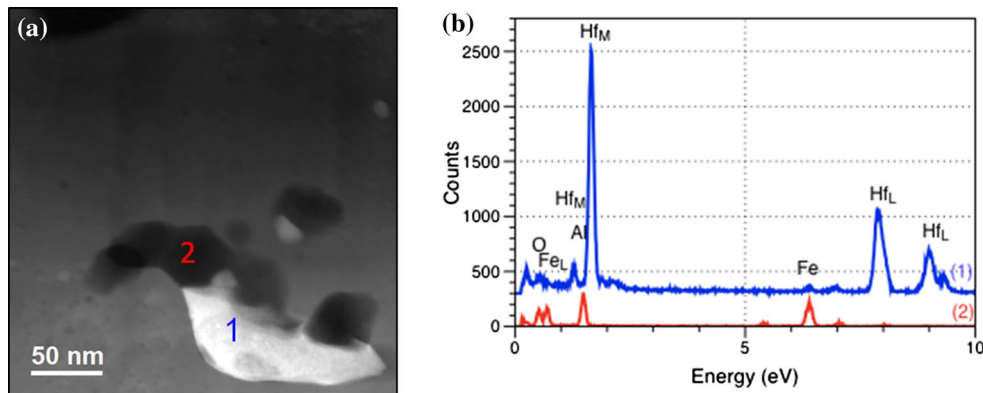Co-nucleation of the different oxide phases was found in all three alloys. In 125Y co-nucleation of

Figure 7 **a** HAADF-STEM image showing large oxide particles found in 125YH alloy with corresponding **b** EDS spectra showing remnant oxide particle that survived 40 h of ball milling. Large bright particle was identified as monoclinic HfO_2 (Hf/O ratio 2.53), while large dark particle was identified as Al_2O_3 (Al/O ratio 1.4).
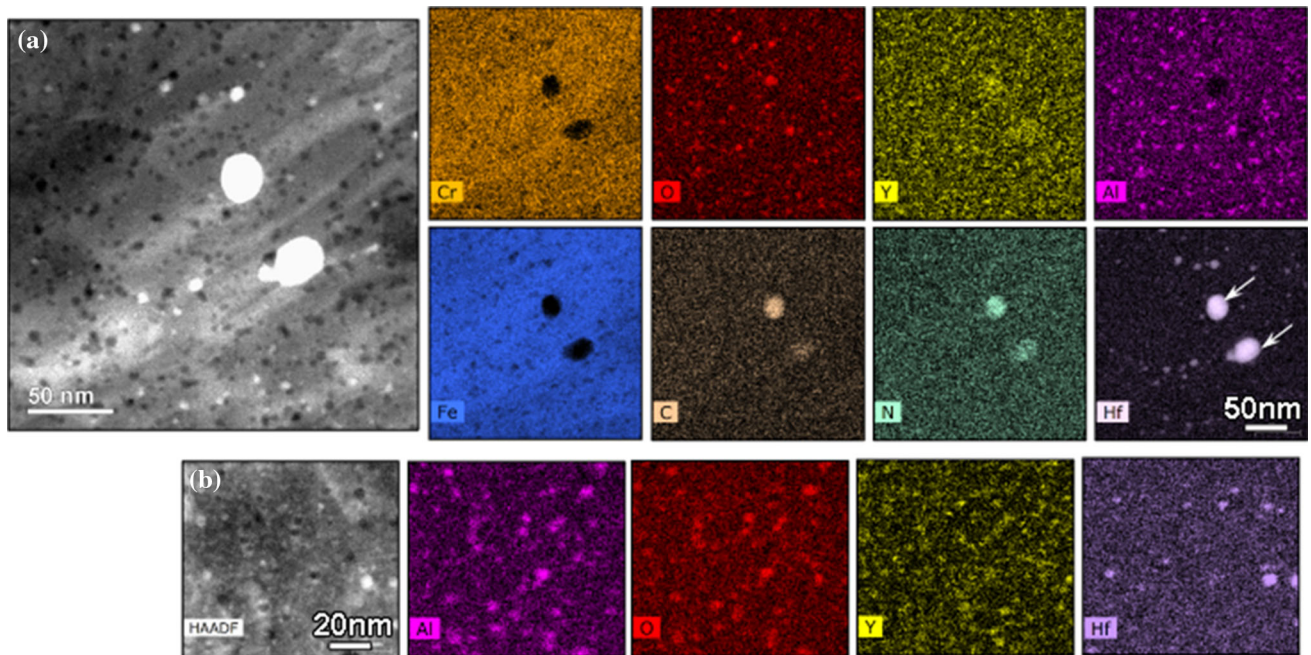
Figure 8 **a** HAADF-STEM image of the as-extruded 125YH (lift-out FIB) microstructure with corresponding **b** EDS elemental maps of Al, O, Y, Cr, Hf, C, N, and Fe.
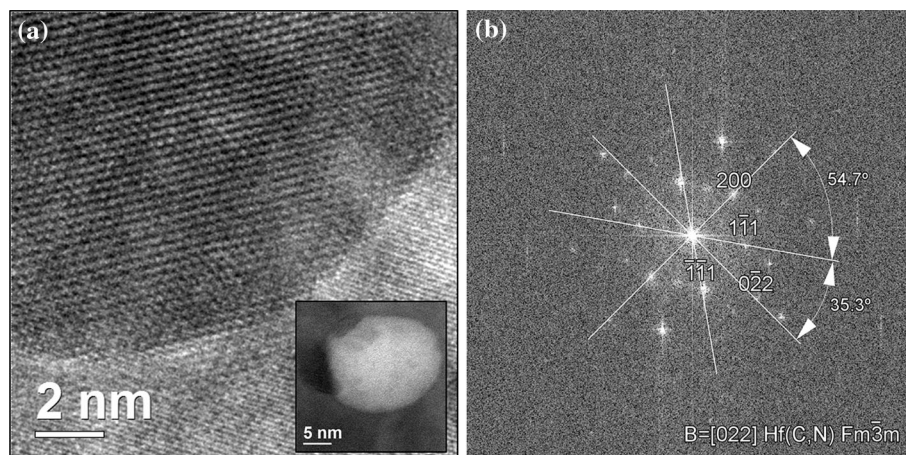

Figure 9 **a** High-resolution BF-STEM image of particle, which exhibited bright contrast in HAADF-STEM image (*inset*) found in 125YH alloy and **b** corresponding FFT. A summary of the measured inter-planar distances and angles of the particle are included in Table 5. The results are consistent with the cubic ($Fm\bar{3}m$) Hf(C,N) phase ICDD (PDF[#] 01-080-4476) file.

$Y_3Al_5O_{12}/Al_2O_3$ (1) was identified, while in 125YZ alloy co-nucleation of $Zr(C,N)/Al_2O_3$ and $Zr(C,N)/Y_3Al_5O_{12}$ (2) and in 125YH alloy HfO_2/Al_2O_3, $Y_2Hf_2O_7/Al_2O_3$ and complex $Y_3Al_5O_{12}/Y_2Hf_2O_7/Hf(C,N)$ or $Al_2O_3/Y_2Hf_2O_7/Hf(C,N)$ (3) were observed. However, to our knowledge, co-nucleation has only been suggested by few authors [14, 29, 30] and has not been observed or mentioned by others [11, 18]. Oxygen is reactive with the additive domains

of Y, Al, Zr, and Hf used in the present study. The nucleation rate of oxide phases will depend on how effectively Y, Zr, and Hf are dispersed in the BCC Fe lattice by ball milling. Since Zr, Y, and Hf were added by ball milling using powders of ZrO_2, HfO_2, and Y_2O_3, it is possible that these elements were not uniformly incorporated and distributed throughout the alloy matrix to form solid solution before extrusion. This means that some of the oxides could have

Table 5 Measured and ICDD (PDF# 01-080-4476) inter-planar distances (*d*) and angle (α) for particle exhibited bright contrast in HAADF formed in 125YH alloy; identified as cubic Hf(C,N) phase with space group $Fm\bar{3}m$ matching ICDD (PDF# 01-080-4476) file

d (Å)	$d_1(1\bar{1}1)$	$d_2(200)$	$d_3(0\bar{2}2)$	α_{12} (°)	α_{23} (°)	α_{32} (°)
Measured	2.632	2.392	1.610	54.7	35.3	33.0
Hf(C,N)	2.693	2.333	1.649	54.7	35.3	35.3

retained "as added form" in the BCC Fe matrix before extrusion, while Al was added by Ar gas atomization, which produced a uniform distribution of Al throughout the matrix and formed a solid solution with Fe. Additionally, a higher amount of Al (5 wt%) was added in each alloy than Y (~0.18 wt%), Zr (0.3 wt%), or Hf (0.68 wt%) to enhance Al_2O_3 scale formation. The 5 wt% Al level indicates that approximately 1 in 10 atoms is Al, or for every 5 unit cells there should be an Al atom in random solid solution. Thus, Al has a much shorter distance to diffuse in order to react with an O atom compared to oxides dependent on Y, Zr, or Hf. Moreover, the diffusion rates of the elements in the BCC Fe matrix will also influence the nucleation rate of the oxide phases. Al has a similar diffusion rate as self-diffusion of Fe in the BCC matrix enhancing further reaction with O over other elements. Hf and Zr are the slowest diffusers in BCC Fe matrix, which can further impede oxide formation and distribution.

Finally the O level can also contribute to the amount and distribution of the oxides formed within the alloy and influence the reaction kinetics with available reactive solute atoms. More O was present in both 125YZ and 125YH alloys than in the 125Y alloy, which agreed with the higher number density of oxide particles formed in these two alloys compared to 125Y. This shows the dependence between
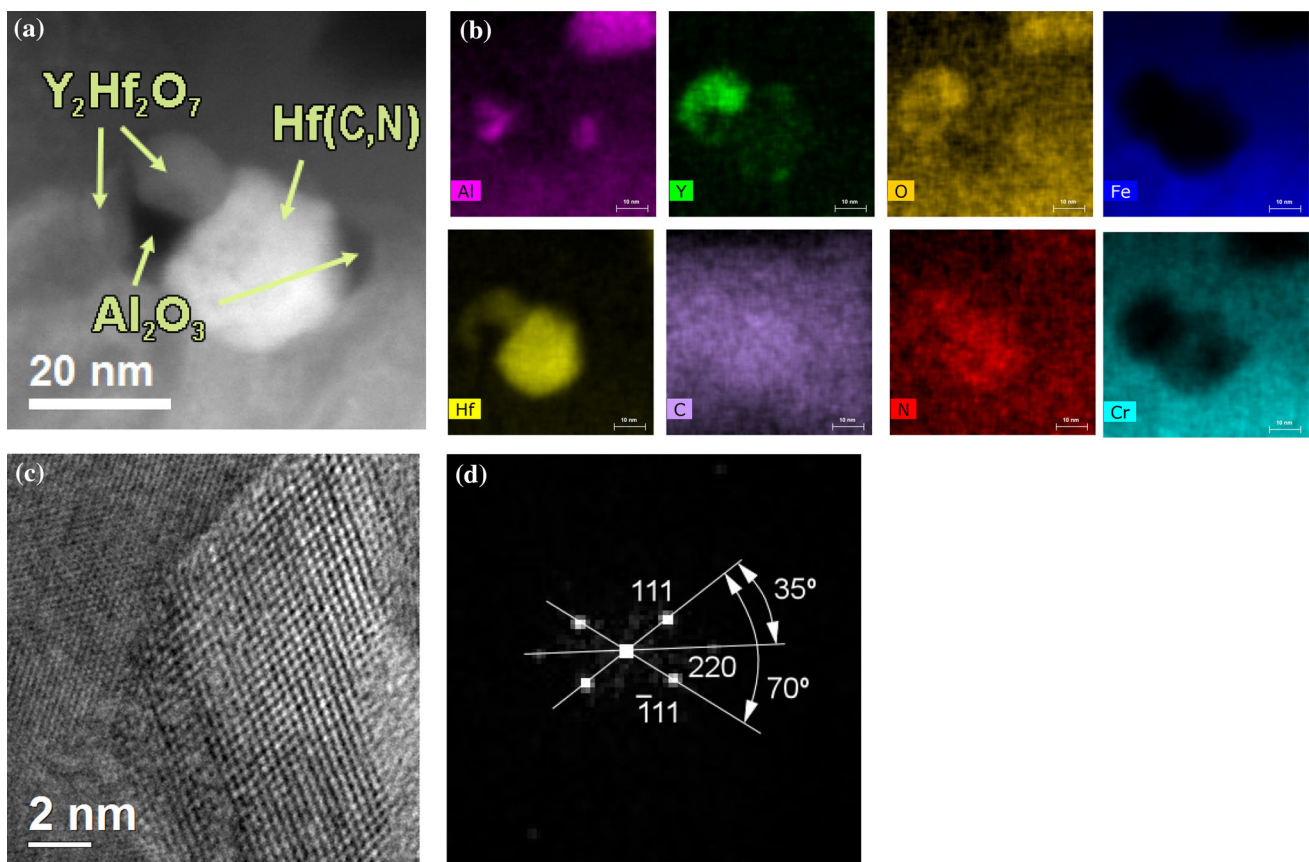

Figure 10 a HAADF-STEM image of the co-nucleated oxide particles formed in 125YH showing larger (~50 nm) bright particle with 5 nm in size mixture of gray and dark particles. **b** EDS elemental maps of Al, Y, O, Fe, Hf, C, N, and Fe. **c** High-resolution BF-STEM image of the particle, which exhibited gray contrast in HAADF-STEM image, with corresponding. **d** FFT generated from the high-resolution BF-STEM image 10c with measured angles and *d*-spacing that fits $Y_2Hf_2O_7$ ($Fd\bar{3}m$ space group).

Table 6 Measured and ICSD (PDF# 04-001-9353) inter-planar distances (d) and angle (α) for co-existing oxide precipitate exhibited bright contrast in HAADF in 125YH alloy

d (Å)	$d_1(1\bar{1}1)$	$d_2(220)$	α_{12} (°)	α_{11} (°)
Measured	2.950	1.820	35	70
$Y_2Hf_2O_7$	2.985	1.828	35.27	70.52

Oxide identified as $Y_2Hf_2O_7$ with space group $Fm\bar{3}m$ with a = 5.17

the O level and precipitate density. In addition, the quantities of Hf and Zr reduced the size of oxide particles within grain interiors and at the grain

boundaries [5, 11]. All of these factors contribute to preferential formation of Al_2O_3, which seems to be a nucleation site for other phases resulting in the co-precipitation with the exception of HfO_2 remnant from fabrication of the alloys.

The existence of carbo-nitrides can be explained by considering the effects of ball milling. One possibility that agrees with our results is that the ZrO_2 powder was effectively broken down by ball milling, forcing the Zr and O into solution in the BCC Fe lattice. Since ZrC is a very stable carbide [33], the Zr(C,N) then nucleated based on preferential reaction of Zr with C (and N). The same will be true for HfO_2, where some of the HfO_2 oxides from the powder were effectively

Figure 11 a HAADF-STEM image with corresponding **b** electron diffraction pattern of the large dark contrast particles in 125YH. The summary of the measured inter-planar distances and angles of the particle are included in Table 7. The results are consistent $Ia3d$ $Al_5Y_3O_{12}$ (YAG phase) matching ICDD (PDF# 33-0040).
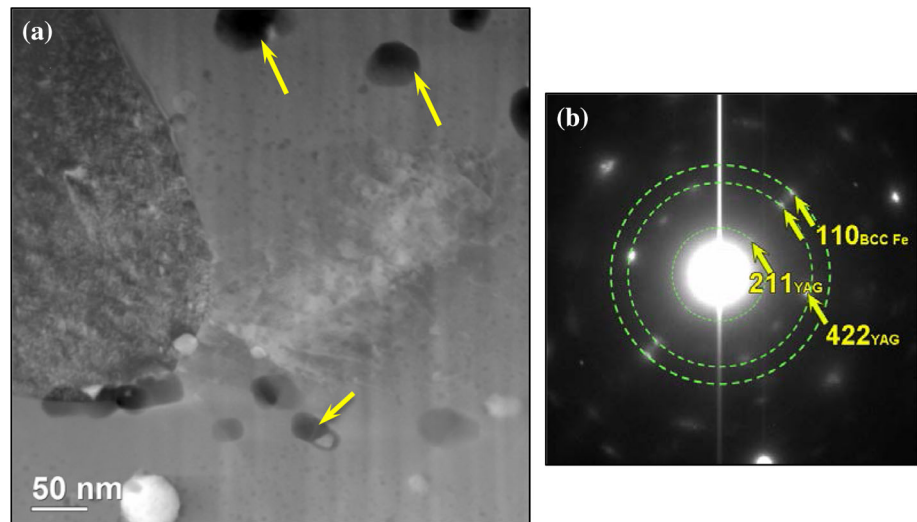

Table 7 Measured and ICDD (PDF# 33-0040) inter-planar distances (d) for 125YH alloy

$d_{measured}$ (Å)	d_{tabled} (Å)	Reflections	Stoichiometry	Space groups
3.03	3.002	(400)	$Al_5Y_3O_{12}$ (YAG)	$Ia\bar{3}d$
2.70	2.687	(420)	$Al_5Y_3O_{12}$ (YAG)	$Ia\bar{3}d$
2.59	2.561	(332)	$Al_5Y_3O_{12}$ (YAG)	$Ia\bar{3}d$
2.56	2.561	(332)	$Al_5Y_3O_{12}$ (YAG)	$Ia\bar{3}d$
2.11	2.122	(440)	$Al_5Y_3O_{12}$ (YAG)	$Ia\bar{3}d$
2.02	2.027	(332)	Fe	BCC

Table 8 Summary of the oxides and particles found in 125Y, 125YZ, and 125YH alloys

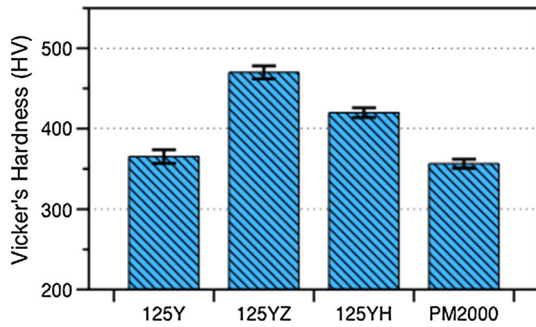| 125Y	125YZ	125YH
Nano-size dark oxides	Nano-size dark oxides	Nano-size dark oxides
$Y_3Al_5O_{12}$ (YAG) (Iad)	$Y_3Al_5O_{12}$ (YAG) (Iad)	$Y_3Al_5O_{12}$ (YAG) (Iad)
Al_2O_3	Al_2O_3	Al_2O_3
	Zr(C,N)	Hf(C,N)
		$Y_2Hf_2O_7$ ($Fd\bar{3}m$)

Figure 12 Vickers hardness measurements of mechanically alloyed and extruded 125Y, 125YZ, and 125YH. For comparison the results for PM2000 are also included.

broken down by ball milling and resulted in Hf(C,N) nucleation, since HfC are stable carbides. However, the question is why there is a higher number of HfO_2 particles were observed in 125YH. First of all, Hf has a lower solubility (0.01 at%) in BCC Fe than Zr (0.1 at%) [20], which can cause precipitation out of HfO_2. Secondly, most likely HfO_2 required higher milling energy to be broken down in order to be incorporated in the BCC Fe matrix. This could be avoided using gas-atomized powder containing Hf for mechanical alloying. Further, Al_2O_3–Hf_2O phase diagram also indicates that the most stable two phases are monoclinic HfO_2 and α-Al_2O_3.

Nevertheless, co-nucleated Zr(C,N) in 125YZ and Hf(C,N) in 125YH were uniformly distributed, unlike reports by Kasada et al. [14] who found mainly $M_{23}C_6$ carbides as inhomogeneous stringer-like precipitates aligned on the grain boundaries in the longitudinal direction. This benefits our alloys and may avoid/minimize anisotropic deformation and fracture behavior of the ODS ferritic steels [34].

Correlation with thermodynamic models and diffusion couples

Thermodynamic models and experimental diffusion couples of ternary oxide systems of Al_2O_3–Y_2O_3–ZrO_2 and Al_2O_3–Y_2O_3–HfO_2 predicted various oxide phases that may form in the materials when modified with Zr or Hf elements [35]. Thermodynamic models predicted the formation of rhombohedral Al_2O_3 (AL), cubic $Al_5Y_3O_{12}$ (YAG), monoclinic $Al_2Y_4O_9$ (YAM), orthorhombic $AlYO_3$ (YAP) phases in both ODS alloys with additional phase of cubic ZrO_2 (F) in Zr-rich alloy and cubic $Y_2Hf_2O_7$ in Hf-rich alloy. In

diffusion couple studies, however, fewer phases were found than predicted. In addition to the YAG phase found in both alloys, only $Y_4Zr_3O_{12}$ was revealed in the Zr-rich alloy and $Y_2Hf_2O_7$ was found in the Hf-rich alloy. The following phases were found in the three ODS FeCrAl alloys: rhombohedral Al_2O_3 (AL) and cubic $Al_5Y_3O_{12}$ (YAG), and additionally Zr(C,N) in 125YZ, and Hf(C,N), HfO_2 and $Y_2Hf_2O_7$ in 125YH. Some differences between diffusion couple results and ODS alloys such as absence of phases (no indication of coherent trigonal δ-phase $Y_4Zr_3O_{12}$ oxides, even though it was found by Dou et al. [10], nor $Y_2Zr_2O_7$ found by Yu et al. [11], or tetragonal or cubic ZrO_2 in 125YZ) or existence of additional phases [HfO_2, Hf(C,N) in 125YH or Zr(C,N) in 125YZ] may rise due to the presence of BCC Fe matrix and impurities (due to alloy processing). Diffusion couple studies and thermodynamic models considered only interactions between the oxides. The absence of BCC Fe matrix avoids the solubility limits that may play a key role in precipitation and explain presence and/or absence of mentioned phases. Both of the elements (Hf and Zr) have low solubility in BCC Fe matrix with Hf being the lowest (0.01 at%), which could explain the additional presence of HfO_2 in the Hf-rich alloy. As previously mentioned, finding this phase in the alloy strongly suggests that the large HfO_2 particles were most likely remnants of the oxide particles that were not fully incorporated into the solid solution of the pre-alloyed powder during ball milling. To confirm this theory, gas-atomized powders with incorporated Hf are being produced and will be compared with 125YH alloy.

Moreover, the presence of large Al_2O_3 particles is associated with their formation during processing (either ball milling or extrusion). The presence of Al_2O_3 might further affect the Al content in the matrix causing its depletion and subsequent particle growth, which might be detrimental to the mechanical properties and cause stress concentrations that decrease the fracture toughness, and further decrease the availability of Al for protection by the formation of an Al_2O_3 surface scale at high temperatures. The opposite was found with Y_2O_3; no Y_2O_3 particles were found in the 125YZ and 125YH alloys indicating that 40-h ball milling was sufficient for these oxide particles to be fully solutionized in the alloy. From this characterization study of the three alloys, oxide particles of the monoclinic $Al_2Y_4O_9$ (YAM) or orthorhombic $AlYO_3$ (YAP) were not found. This

does not exclude their presence in the alloys, since they may have been missed due to challenges in analyzing a larger number of nano-size oxide particles or they may form during longer aging times at high temperatures if favored thermodynamically. Our study evidently shows that many factors can influence the outcome of the oxide phase formation that need to be included in the thermodynamic modeling. Also, small changes in processing or alloy composition can cause large variation in the microstructure [10, 11, 18].

The effects of Zr and Hf on other microstructural features

A comparison of the grain size between the three ODS FeCrAl alloys revealed that the Zr addition significantly reduced the grain size (3.1 reduction factor). Additionally, the 125YZ alloy with the Zr addition had the highest total number density of precipitates (2.51×10^{23} m^{-3}) versus 125Y (1.41×10^{23} m^{-3}) and 125YH (2.32×10^{23} m^{-3}). There was also a noticeable effect of Zr and Hf additions on the smallest oxide particle size (~ 3 nm) (dark contrast relative to the surrounding matrix in HAADF-STEM images), which were uniformly distributed throughout the matrix in all three alloys. In alloy 125YZ and 125YH, the average diameter was larger (2.91 ± 1.43 and 3.18 ± 2.29 nm, respectively) than in alloy 125Y (2.43 ± 1.40 nm). Particles with a slightly larger size but still in the nano-size range will result in stronger barrier to dislocation motion, causing an increase in the strength of the material. A higher density of these oxide particles with larger sizes ($d \cong 10.2 \pm 5.8$ nm for 125YZ, $d \cong 10.6 \pm 11.2$ nm for 125Y, and $d \cong 31.0 \pm 18.2$ nm for 125YH) than the ones in the matrix was found at the grain boundaries in 125YZ compared to the other two alloys. It is generally recognized that high kinetic energy ball milling can reduce the grain size in alloyed powders to <50–100 nm, which means that coarsening of the grain size occurs during extrusion at high temperatures. The presence of these grain boundary oxide precipitates, which form by heterogeneous nucleation at the grain boundaries, contributed to the smaller grain size in 125YZ by hindering subsequent grain growth. At room temperature, the highest Vicker's hardness was measured in the alloy with Zr addition, while the lowest hardness was measured in the 125Y alloy. Results from tensile testing [16] showed that at room temperature the yield and ultimate strength were higher for both 125YZ ($\sigma_{ys} = 1236$ MPa and $\sigma_{uts} = 1316$ MPa, respectively) and 125YH ($\sigma_{ys} = 1203$ MPa and $\sigma_{uts} = 1309$ MPa, respectively) alloys than for 125Y alloy ($\sigma_{ys} = 1017$ MPa and $\sigma_{uts} = 1117$ MPa, respectively). This suggests that the presence of a high density of YAG particles at the grain boundaries has a major contribution in the increasing the strength of the material due to first restraining grain growth, which results in the small grain size, and subsequently the small grain size further provides grain boundary strengthening causing the increase in strength and hardness of the 125YZ alloy. The small nano-size YAG oxides contribute to precipitation hardening, but their distribution is very similar with small variation in the average size. A similar precipitation hardening effect in all three alloys can be associated with the dispersion of YAG particles. However, additional precipitates within the alloy like Zr(C,N) in 125YZ and $Y_2Hf_2O_7$, Hf(C,N), and HfO_2 in 125YH may contribute additionally to hardening triggering an increase in strength. Other factors like grain matrix and dislocation forest hardening should also be considered as other hardening sources in the future, but based on the similarities and differences of the microstructure and mechanical properties, grain boundary strengthening and precipitation hardening are considered to provide the most to the high-strength properties of the ODS FeCrAl alloys.

The beneficial effect of Zr has also been found by Dou et al. [10], Yu et al. [11] and Ohnuki et al. [18], where a smaller grain size was found with the addition of Zr as well as smaller size and higher number density of oxides due to the low-oxide energy formation [18] for both Hf and Zr oxides. This shows that a chain reaction where the size of the oxides (small) and their density (high) strongly restricts grain growth causing an increase in mechanical properties, which are further improved via grain boundary strengthening. Additionally, a higher total number density of oxides and carbo-nitride particles was measured in our study than was measured by either Dou et al. [10] (7.16×10^{22} in Fe–14.85Cr–1.84W–0.09Ti–3.73Al–0.63Zr (wt%)) or Yu et al. [11] (2.0×10^{22} in Zr-ODS steel and 2.5×10^{22} in Hf-ODS steel), which also was reflected in higher values of hardness measurements as well as in yield and ultimate strength.

Potential benefit of the microstructures obtained in 125YZ and 125YH

One of the main purposes of introducing the oxide particle dispersion is to increase resistance to irradiation damage by forming a high number density of sinks for point defects that are uniformly distributed throughout the matrix, while improving oxidation resistance by adding Al. Thus, the high number density of particles in alloys 125YZ and 125YH are very promising and could be beneficial in improving the radiation resistance. To confirm this theory, current investigation is being conducted to evaluate the irradiation behavior of the ODS Fe–12Cr–5Al alloys after applying two different scenarios: sequential irradiations (500–1000 ppma He at 650 °C followed by $\sim$50 dpa Fe at 650 °C) and dual beam irradiation (6.4 MeV Fe^{3+} and 1 MeV He^+). Even though the Zr addition is recommended over the Hf addition in terms of thermal neutron cross-section area or neutron absorption [5], the 125YH alloy is added due to scientific interests and to compare with 125YZ.

Conclusions

Advanced characterization of the microstructure of three mechanically alloyed ODS Fe–12Cr–5Al with additions of Y_2O_3, $Y_2O_3 + ZrO_2$, and $Y_2O_3 + HfO_2$ showed the presence of nano-grained structures in all three materials. The smallest grain size, the highest tensile properties, and Vickers hardness at room temperature were found in alloy 125YZ suggesting that the Zr addition has the strongest effect. In all three extruded ODS alloys, nano-size ($\sim$3 nm) oxide precipitates consistent with the existence of either $Y_3Al_5O_{12}$ or Al_2O_3 were found, which was confirmed by Fe-jump ratio images, EDS analysis, and dark contrast in HAAD-STEM mode images combined with FFT and SAED analysis. Also, the cubic $Y_3Al_5O_{12}$ YAG (<20 nm) and Al_2O_3 phases were found, while Zr(C,N) was additionally identified in 125YZ alloy and $Y_2Hf_2O_7$, Hf(C,N) and HfO_2 were found in 125YH alloy.

Acknowledgements

References

[[1] Zinkle SJ, Snead LL (2014) Designing radiation resistance in materials for fusion energy. Annu Rev Mater Res 44:241–267

[2] Certain A, Kuchibhatla S, Shutthanandan V, Hoelzer DT, Allen TR (2013) Radiation stability of nanoclusters in nano-structured oxide dispersion strengthened (ODS) steels. J Nucl Mater 434:311–321

[3] Yamamoto T, Odette GR, Miao P, Hoelzer DT, Bentley J, Hashimoto N, Tanigawa H, Kurtz RJ (2007) The transport and fate of helium in nanostructured ferritic alloys at fusion relevant He/dpa ratios and dpa rates. J Nucl Mater 367–370:399–410

[4] Field KG, Hu X, Littrell KC, Yamamoto Y, Snead LL (2015) Radiation tolerance of neutron-irradiated model FeCrAl alloys. J Nucl Mater 465:746–755

[5] Kimura A, Kasada R, Iwata N, Kishimoto H, Zhang CH, Isselin J, Dou P, Lee JH, Muthukumar N, Okuda T, Inoue M, Ukai S, Ohnuki S, Fujisawa T, Abe TF (2011) Development of Al added high-Cr ODS steels for fuel cladding of next generation nuclear systems. J Nucl Mater 417:176–179

[6] Unocic KA, Pint BA (2014) Alloying and coating strategies for improved Pb–Li compatibility in DEMO-type fusion reactors. J Nucl Mater 455:330–334

[7] Takaya S, Furukawa T, Aoto K, Müller G, Weisenburger A, Heinzel A, Inoue M, Okuda T, Abe F, Ohnuki S, Fujisawa T, Kimura A (2009) Corrosion behavior of Al-alloying high Cr-ODS steels in lead–bismuth eutectic. JNM 386–388:507–510

[8] Stoloff NS (1966) In: Fracture: proceedings of conference on the physical basis of yield and fracture. Physical Society, London, p 68–76

[9] Furukawa T, Ohtsuka S, Inoue M, Okuda T, Abe F, Ohnuki S, Fujisawa T, Kimura A (2009) Super ODS steels R&D for

fuel cladding of next generation nuclear systems 4) mechanical properties at elevated temperatures. Proc ICAPP 2009:2204–2210

[10] Dou P, Kimura A, Kasada R, Okuda T, Inoue M, Ukai S, Ohnuki S, Fujisawa T, Abe F (2014) TEM and HRTEM study of oxide particles in an Al-alloyed high-Cr oxide dispersion strengthened steel with Zr addition. JNM 444:441–453

[11] Yu CZ, Oka H, Hashimoto N, Ohnuki S (2011) Development of damage structure in 16Cr–4Al ODS steels during electron-irradiation. J Nucl Mater 417:286–288

[12] Zhang CH, Kimura A, Kasada R, Jang J, Kishimoto H, Yang YT (2011) Characterization of the oxide particles in Al-added high-Cr ODS ferritic steels. J Nucl Mater 417:221–224

[13] Alinger MJ, Odette GR, Hoelzer DT (2009) On the role of alloy composition and processing parameters in nanocluster formation and dispersion strengthening in nanostuctured ferritic alloys. Acta Mater 57:392–406

[14] Kasada R, Toda N, Yutani K, Cho HS, Kishimoto H, Kimura A (2007) Pre- and post-deformation microstructures of oxide dispersion strengthened ferritic steels. J Nucl Mater 367:222–228

[15] Unocic KA, Hoelzer DT, Pint BA (2015) Microstructure and environmental resistance of low Cr ODS FeCrAl. Mater High Temp 32:123–132

[16] Pint BA, Dryepondt S, Unocic KA, Hoelzer DT (2014) Development of ODS FeCrAl for compatibility in fusion and fission energy applications. JOM Mag 66:2458–2466

[17] Takaya S, Furukawa T, Müller G, Heinzel A, Jianu A, Weisenburger A, Aoto K, Inoue M, Okuda T, Abe F, Ohnuki S, Fujisawa T, Kimura A (2012) Al-containing ODS steels with improved corrosion resistance to liquid lead–bismuth. J Nucl Mater 428:125–130

[18] Ohnuki S, Hashimoto N, Ukai S, Kimura A, Inoue M, Kaito T, Fujisawa T, Okuda T, Abe F (2009) Super ODS steels R&D for fuel cladding of next generation nuclear systems 2) effect of minor alloying elements. In: Proceedings of the ICAPP 2009

[19] Mazzoni AD, Conconi MS (2002) Synthesis of group IVB metals oxicarbides by carboreduction reactions. Mater Res 5:459–466

[20] Arias D, Abriata JP (1988) The Fe–Zr (iron–zirconium) system. Bull Alloy Phase Diagr 9:597–604

[21] Dawson K, Tatlock GJ (2014) Characterisation of nanosized oxides in ODM401 oxide dispersion strengthened steel. J Nucl Mater 444:252–260

[22] Wasilkowska A, Bartsch M, Messerschmidt U, Herzog R, Czyrska-Filemonowicz A (2003) Creep mechanisms of ferritic oxide dispersion strengthened alloys. J Mater Process Technol 133:218–224

[23] Schneibel JH, Heilmaier M, Blum W, Hasemann G, Shanmugasundaram T (2011) Temperature dependence of the strength of fine- and ultrafine-grained materials. Acta Mater 59:1300–1308

[24] Dubiel B, Wróbel M, Ennis PJ, Czyrska-Filemonowicz A (1997) Microstructure of INCOLOY MA956 after low and high temperature deformation. Scr Mater 37:1215–1220

[25] Czyrska-Filemonowicz A, Clemens D, Quadakkers WJ (1995) The effect of high temperature exposure on the structure and oxidation behaviour of mechanically alloyed ferritic ODS alloys. J Mater Process Technol 53:93–100

[26] Czyrska-Filemonowicz A, Dubiel B (1997) Mechanically alloyed, ferritic oxide dispersion strengthened alloys: structure and properties. J Mater Process Technol 64:53–64

[27] Krautwasser P, Czyrska-Filemonowicz A, Widera M, Carsughi F (1994) Thermal stability of dispersoids in ferritic oxide-dispersion-strengthened alloys. Mater Sci Eng A 177:199–208

[28] Konys J, Krauss W, Voss Z, Wedemeyer O (2007) Comparison of corrosion behavior of bare and hot-dip coated EUROFER steel in flowing Pb–17Li. J Nucl Mater 367–370:1144–1149

[29] Klimenkov M, Moslang A, Lindau R (2008) EELS analysis of complex precipitates in PM 2000 steel. Eur Phys J Appl Phys 42:293–303

[30] Klimiankou M, Lindau R, Moslang A, Schroder J (2005) TEM study of PM 2000 steel. Powder Metall 48:277–287

[31] Dubiel B, Osuch W, Wróbel M, Ennis PJ, Czyrska-Filemonowicz A (1995) Correlation of the microstructure and the tensile deformation of INCOLOY MA956. J Mater Process Technol 53:121–130

[32] Ukai S, Nishida T, Okada H, Okuda T, Fujiwara M, Asabe K (1997) Development of oxide dispersion strengthened ferritic steels for FBR core application (I). J Nucl Sci Technol 34:256–263

[33] Hald J, Korcakova L (2003) Precipitate stability in creep resistant ferritic steels—experimental investigations and modelling. ISIJ Int 43:420–427

[34] Kasada R, Toda N, Cho HS, Kimura A (2005) In: Proceedings of the 2005 international congress on advances in nuclear power plants (ICAPP'05), pp 1703–1711

[35] Pint BA, Hoelzer DT, Shin D, Unocic KA (2012) Development of ODS FeCrAl for fusion reactor applications. Fusion React Mater Program 53:10–14